

A computational framework for large-scale seismic simulations of residential building stock

Original

A computational framework for large-scale seismic simulations of residential building stock / Marasco, Sebastiano; Zamani Noori, Ali; Domaneschi, Marco; Cimellaro, Gian Paolo. - In: ENGINEERING STRUCTURES. - ISSN 0141-0296. - ELETTRONICO. - 244:(2021), p. 112690. [10.1016/j.engstruct.2021.112690]

Availability:

This version is available at: 11583/2914804 since: 2021-08-17T01:38:03Z

Publisher:

Elsevier

Published

DOI:10.1016/j.engstruct.2021.112690

Terms of use:

This article is made available under terms and conditions as specified in the corresponding bibliographic description in the repository

Publisher copyright

(Article begins on next page)

A computational framework for large-scale seismic simulations of residential building stock

Sebastiano Marasco¹, Ali Zamani Noori², Marco Domaneschi³, and Gian Paolo Cimellaro^{4*}

ABSTRACT

Urban areas reveal particularly vulnerable due to the high concentration of people and, in many cases, their hazard-prone location. Indeed, according to data from the United Nations, about 2/3 of the population will live in large cities by 2050, and the majority of the world's cities are highly exposed to disasters. This paper presents a computational framework to assess the seismic vulnerability and the damage of residential building portfolio in urban areas. First, a surrogated model is proposed to estimate the global capacity of building structures. Monte Carlo simulations are implemented to take into account the uncertainties associated with the material, mechanical, and geometrical parameters. The proposed approach is validated through nonlinear finite element models and a real case study. Then, the proposed computational framework is implemented and applied to a virtual city that is envisioned for being representative of a typical Italian residential building stock. The main achievement of this work is to introduce a new simplified approach for large scale structural analyses to limit the computational efforts while providing reasonable results.

Keywords: Simulation; Earthquake; Urban area; Capacity curve; Damage assessment.

¹Postdoctoral research associate, Department of Structural, Geotechnical and Building Engineering, Politecnico di Torino, Italy, E-mail: sebastiano.marasco@polito.it.

²Postdoctoral research associate, Department of Structural, Geotechnical and Building Engineering, Politecnico di Torino, Italy, E-mail: ali.zamani@polito.it.

³Assistant Professor, Department of Structural, Geotechnical and Building Engineering, Politecnico di Torino, Italy, E-mail: marco.domaneschi@polito.it.

^{4*} Corresponding author: Visiting Professor, Department of Structural & Environmental Engineering, University of California, Berkeley, Berkeley, USA, E-mail: gianpaolo.cimellaro@polito.it.

21 1. INTRODUCTION

22 Recent disasters have shown the vulnerability of the built environment at the urban scale and
23 how complex the process to improve its resilience is [1-6]. Earthquake response prediction of
24 buildings portfolio requires the use of large-scale simulation methods which are based on
25 statistical and deterministic approaches. In the first case, the building damage assessment is
26 based on statistical data collected from previous seismic events [7]. One widely used method is
27 the Damage Probability Matrix (DPM) which predicts the level of damage for different seismic
28 intensities and buildings typologies [8]. The concept of DPM was widely adopted into the ATC-
29 13 report [9] to evaluate the earthquake damage data for California that includes the DPMs for
30 78 different facility types. Later, Dolce, Kappos [10] applied a modified version of it to the city
31 of Potenza (Southern Italy), while Eleftheriadou and Karabinis [11] extended the DPM-based
32 methodology to the building stock in Southern Europe.

33 On the contrary, deterministic methods are usually based on physical models using nonlinear
34 static or dynamic analyses. The former case may consider the Capacity Spectrum Method, CSM
35 [12], or N2 method [13]. E.g., El Ezz, Nolle [14] adopted the CSM to assess the seismic damage
36 of Quebec City, Canada.

37 Focusing on dynamic approaches, Korkmaz [15] proposed a probabilistic seismic safety
38 assessment performing nonlinear analyses on unreinforced masonry low-rise buildings specific
39 to Pakistan building portfolio. Furthermore, Tang, Lu [16] assessed the collapse resistance of
40 Reinforced Concrete (RC) frame structures representative of the Chinese school stock using
41 Incremental Dynamic Analysis (IDA) [17]. Xu, Lu [18] proposed a high-fidelity structural model
42 to predict the seismic damage on buildings in urban areas. In the context of regional seismic
43 damage simulation, Lu and Guan [19] proposed a shear model for Multi Degree of Freedom
44 (MDOF) systems and a shear-flexure model for tall buildings.

45 The available large-scale simulation models assess the structural seismic damage and
46 vulnerability classifying the buildings into different groups (typological approach). Usually,
47 buildings are grouped based on building archetype, number of stories, seismic design level. For
48 example, the Global Earthquake Model (GEM) [20, 21] consists of an initiative to calculate and
49 communicate earthquake risk worldwide. One of its main components is the development of
50 open-source software for seismic hazard and risk assessment. The vulnerability model is based
51 on a fragility function for each building class contained in the exposure model.

52 Another example of a typological approach was implemented in the WP4 of the RISK-UE
53 project [22], which aims at developing vulnerability and fragility models for the current building
54 stock prevailing the European built environment. The main issues consist of classifying the
55 current building stock, implementing a first level (LM1) approach to assess the vulnerability, and
56 developing a second level (LM2) method to model the building capacity and fragility. The LM1
57 model is based on the definition of the building vulnerability through qualitative damage
58 matrices associated with the European Macroseismic Scale [23]. On the other hand, the LM2
59 method focuses on the quantification of the potential damage experienced by buildings after a
60 given ground shaking. Capacity models are developed for each building class to represent the
61 first mode response based on certain engineering parameters that characterize the nonlinear
62 structural behavior, while capacity curves are idealized as a bilinear function defined by the yield
63 and ultimate control points. The values of shear force and top displacement are determined in the
64 first period of vibration, design strength, overstrength, and ductility parameters. They are
65 identified by code requirements, experimental and empirical evidences, and expert evaluation.
66 The seismic performance of each building class is then evaluated by applying the CSM.

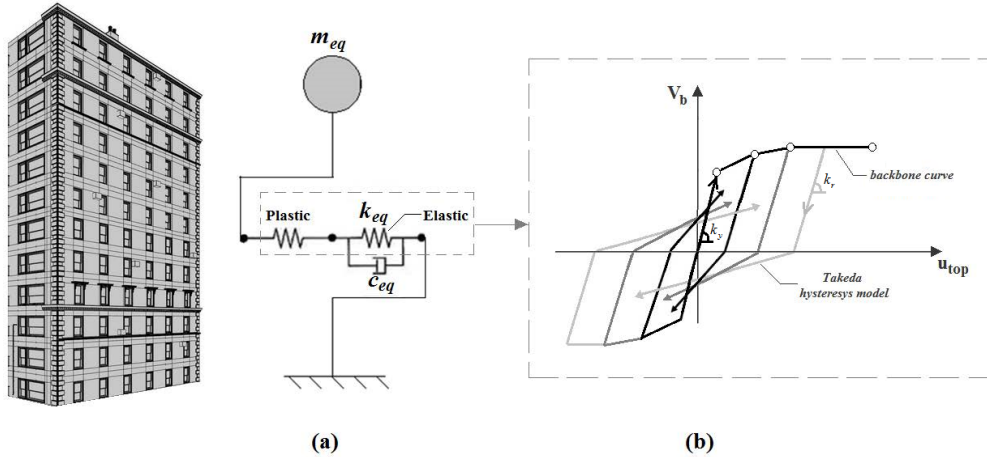
67 Although these approaches provide a rapid and simplified estimate, their results could be not
68 always equivalent to the actual response of the individual building. Indeed, it depends
69 significantly on the number of the involved parameters such as geometry, structural
70 characteristics, materials, etc. On the contrary, refined models allow a better estimation of the
71 seismic response of the individual building but require a large amount of data making the
72 simulation process computationally complex. E.g., Hori, Ichimura [24] developed a project to
73 study the earthquake effects in the urban environment using an Integrated Earthquake Simulation
74 (IES). The input data was collected into a Geographic Information System (GIS) and then
75 converted into suitable numerical models. Examples of applications of IES for Tokyo and
76 Istanbul are presented in [25, 26].

77 This paper proposes a surrogated nonlinear physical model that aims to be at an intermediate
78 level between a detailed description of the built environment, e.g. the IES project [24], and a
79 typological one [18, 20]. The new surrogated model is an equivalent Single Degree of Freedom
80 (SDOF) system used to reproduce the global seismic behavior of each residential building. It
81 allows limiting the computational efforts to a refined finite element (FE) model while predicting
82 the seismic response of an individual building more accurately than an approach based on
83 building classes.

84 The next section of the paper provides a detailed description of the capacity model of buildings.
85 The third section illustrates the damage assessment through nonlinear time history analysis. The
86 fourth section deals with the validation of the whole proposed computational framework. A real
87 case study is then considered to validate the proposed approach. Finally, in the last section, a
88 large-scale urban simulation is implemented.

89 **2. BUILDING MODELLING**

90 A new surrogated SDOF model is herein proposed to simulate the seismic response and assess
 91 the damage experienced by buildings during a seismic event (Fig. 1a). A backbone curve is
 92 implemented as representative of the global capacity of an individual building, whereas the
 93 strength degradation is accounted through a hysteresis model (Fig. 1b).



94 Fig. 1. Proposed surrogated SDOF model (a) and hysteresis model used to simulate the global
 95 dynamic buildings' behavior of RC buildings
 96

97
 98 The surrogated model adopts as response parameters the roof displacement at the center of mass
 99 [13] and the base shear [27]. The SDOF stiffness is characterized by the equivalent initial elastic
 100 stiffness k_{eq} [28] following by the post-elastic behavior. This last is assessed through the
 101 application of the kinematic theorem of limit analysis by considering different possible collapse
 102 mechanisms. The equivalent mass m_{eq} of the building is computed based on the contributions of
 103 each mode of vibration (Eq. (1)) [29].

104
$$m_{eq} = \Gamma_i \cdot m \cdot \phi_i \quad (1)$$

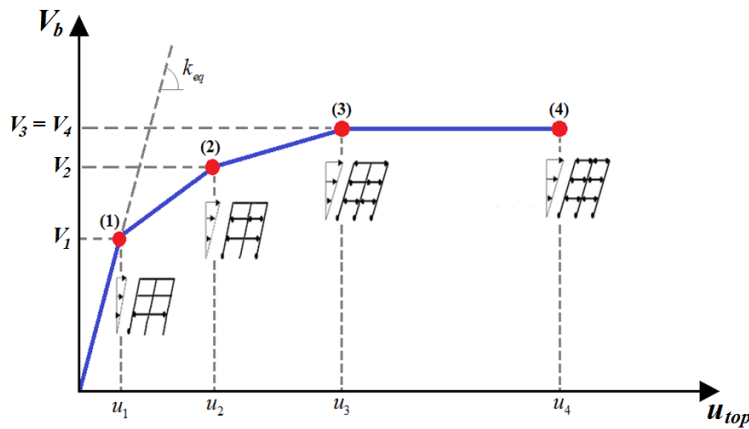
105 where ϕ_i and Γ_i are the natural vibration mode and the modal participation factor of the i^{th}
 106 mode, respectively. Parameter m represents the mass matrix of the building assumed as a
 107 lumped-mass system. All modes having a modal contribution greater than 5 % in the considered

108 direction have been considered. Furthermore, the equivalent damping c_{eq} is evaluated according
 109 to the Rayleigh formulation by assuming the two predominant frequencies and setting a 5%
 110 damping ratio.

111 The capacity of each building is simulated through a four-linear and a tri-linear backbone curves
 112 for RC and masonry buildings, respectively. The first ones have been assumed for RC buildings
 113 to better capture the gradually degrading stiffness that starts from the yield point up to perfectly
 114 plastic response. The hysteretic behavior is reproduced by Takeda, Sozen [30] model adopting
 115 the unloading slope k_u equal to the elastic loading k_y (Fig. 1b).

116 2.1 Capacity model for RC frame building

117 A four-linear backbone curve is assumed to reproduce the global seismic response (Fig. 2) where
 118 V_b is the base shear and u_{top} the top displacement. The first point of the backbone curve (1)
 119 indicates the yield point which refers to the formation of the first plastic hinge in the weakest
 120 column. Then, the global stiffness decreases until the weakest column reaches its maximum
 121 capacity (2). The frame is then subjected to a massive distribution of the internal actions that are
 122 described by a further stiffness decrease. The maximum global capacity is reached at point (3),
 123 from where the structure is subjected to a plastic mechanism until collapse (4).



124

125 Fig. 2. Proposed four-linear backbone curve, representative of the global capacity of RC
126 buildings

127 *2.1.1 Computation of point (1): elastic parameters*

128 The RC building is modeled as a bending type MDOF system with lumped masses. Different
129 methods can be employed to include modal effects in pushover analysis [31], such as those
130 specified in FEMA 356 [32] for a first-mode dominant response, or in Chopra and Goel [29] for
131 Modal Pushover Analysis (MPA). Kunnath [33] proposed a modal combination procedure that
132 involves appropriate modes. Therefore, the lateral force F_i applied at the i^{th} floor related to j^{th}
133 mode is computed as follows (Eq. (2)):

$$134 \quad F_i = \sum_{j=1}^{dof} \pm \alpha_j \cdot \Gamma_j \cdot m \cdot \phi_{ij} \cdot S_{a,j}(\zeta_j, T_j) \quad (2)$$

135 The factor α_j is a modification factor that controls the relative effects of j^{th} mode, Γ_j and ϕ_j are
136 the j^{th} modal participation factor and modal shape, respectively. Parameter m is the total mass,
137 while $S_{a,j}$ represents the maximum spectral acceleration of the corresponding mode.

138 Following Kunnath [33], a method of the weighted average of the individual mode is herein
139 proposed, while the modification factor and the direction of the mode are neglected. These
140 simplifications lead to consider a number of modes n_d less than dof (Eq. (3)).

$$141 \quad \Phi_{eq} = \sum_{i=1}^{n_d} \Gamma_i \cdot \{\Phi_i\} \quad (3)$$

142 Furthermore, the horizontal load pattern is considered to be proportional to the elastic story
143 forces (Eq. (4)) by α coefficient that is monotonically increased to perform the pushover
144 analysis.

$$145 \quad \{F\} = \alpha [K_R] \{\Phi_{eq}\} \quad (4)$$

146 where $[K_R]$ represents the stiffness matrix by Guyan [34]. The yielding point (u_l, V_l) is identified
147 when the maximum allowable internal stress is reached in the most stressed column.

148 **2.1.2 Post-elastic parameters (Points (2), (3), and (4))**

149 In the following, the post-elastic behavior of the backbone curve is presented through an inverse
150 approach.

151 *Maximum shear capacity (V_4)*

152 The maximum shear capacity ($V_3=V_4$; Fig. 2) is estimated through the kinematic theorem of limit
153 analysis that requires the evaluation of different collapse mechanisms [35]. In the proposed
154 methodology, three elementary failure mechanisms are considered: *floor*, *beam*, and *multistory*
155 mechanisms [35]. The floor mechanism is identified by plastic hinges formation at the top and
156 bottom of the columns at a certain story level, while the multistory mechanism consists of a
157 global collapse mechanism. When the collapse mechanism is due to the formation of plastic
158 hinges at the beam-joints and within its span, a beam mechanism occurs. The collapse multiplier
159 (λ) is evaluated by imposing the equivalence of the external virtual work and the internal one
160 considering the generation of elementary collapse mechanisms and on their linear combination
161 [36].

162 Given the yield capacity of each structural member, the collapse multiplier associated with the
163 three selected elementary mechanisms is resumed in Fig. 3. The parameter i refers to the i^{th} story,
164 while j identifies the j^{th} weakest story where plastic hinges form. $M_{c,y,i}$ and $M_{b,y,i}$ are the yield
165 moments of the i^{th} story columns and beams, respectively.

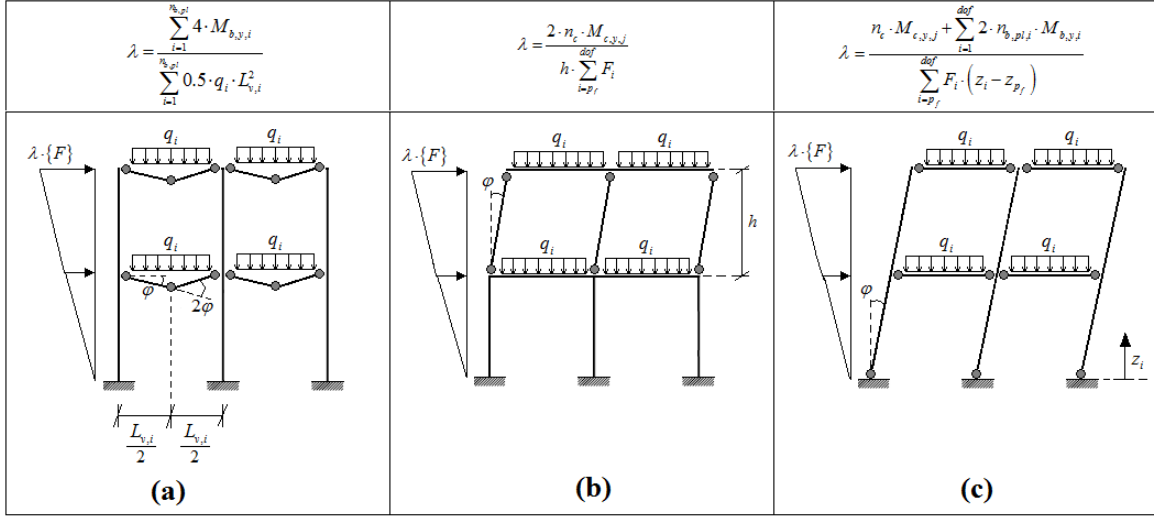


Fig. 3. Beam (a) floor (b) and multistory (c) collapse mechanism and associated collapse multiplier of a RC building

166
167
168

169 Coefficients n_c and $n_{b,pl,i}$ (Fig. 3) represent the number of plastic hinges in the columns and
170 beams for the i^{th} story level, respectively, while ϕ is the plastic rotation. The minimum collapse
171 multiplier is selected among the combination of elementary collapse mechanisms and the
172 maximum shear capacity is given as follow

173
$$V_3 = V_4 = \lambda \cdot V_1 \quad (5)$$

174 *Ultimate collapse displacement (u_4)*

175 The ultimate displacement capacity (u_4) is evaluated through the geometrical model in Fig. 4.
176 The related mathematical expression is given in Eq. (6).

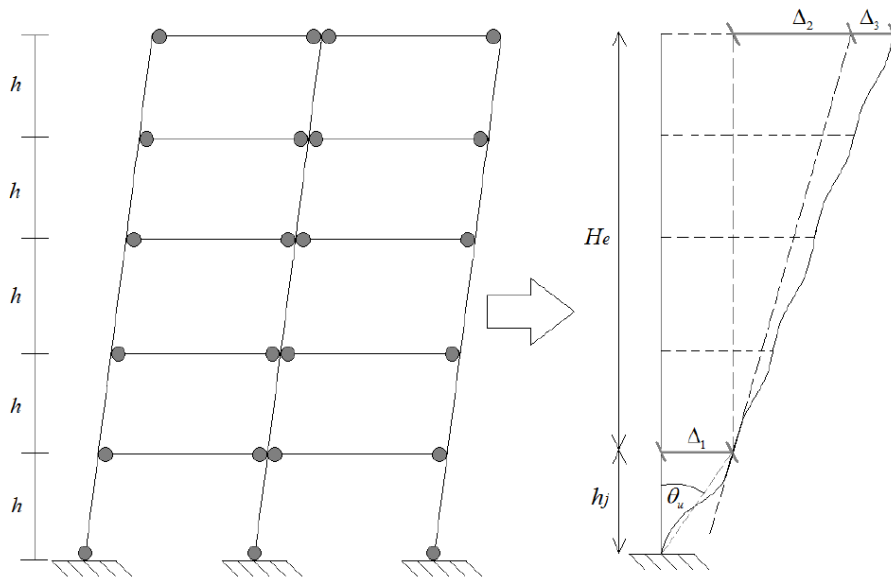
177
$$u_4 = \Delta_1 + \Delta_2 + \Delta_3 = \theta_u \cdot h_j + H_e \cdot \left(\theta_u - \frac{F_j \cdot h_j^2}{3 \cdot E_j \cdot I_j} \right) + \{\phi_{eq}\} \cdot u_1 \quad (6)$$

178 where Δ_1 represents the top column displacement due to the formation of the plastic hinge at the
179 base of the weakest column, while Δ_2 is the horizontal displacement at the top of the building due
180 to the rotation on the top of the weakest column (Fig. 4). The top displacement (Δ_3) represents
181 the elastic contribution that is proportional to the equivalent modal shape multiplied by the yield

182 top displacement. Index j refers to the weakest story level, H_e is the effective building height
 183 (from the weakest level to the top of the building), while θ_u is the ultimate chord rotation
 184 estimated according to [37] (Eq. (7)):

$$185 \quad \theta_u = \varphi_y \cdot \frac{L_v}{3} + (\chi_u - \chi_y) \cdot L_{pl} \cdot \left(1 - \frac{0.5 \cdot L_{pl}}{L_v}\right) \quad (7)$$

186 where φ_y represents the yield rotation of the weakest column, L_v is the shear length of the
 187 weakest column which is assumed to be equal to half column length. The length of the plastic
 188 hinge (L_{pl}) is fixed as 10 % of the shear length, while χ_u and χ_y identify the ultimate and yield
 189 curvature of the weakest column.



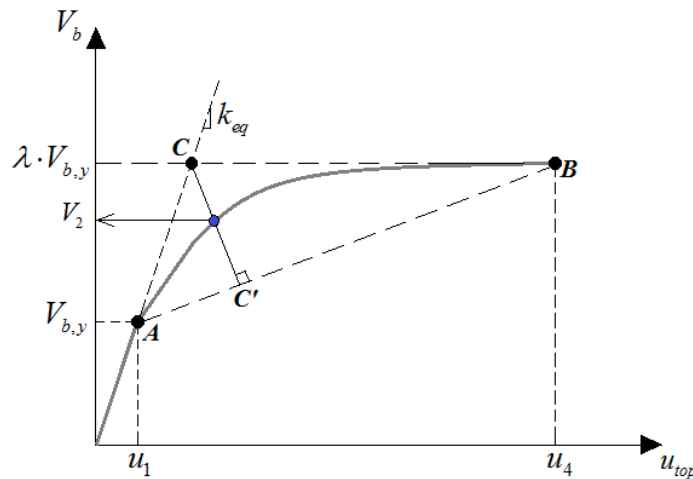
190
 191 Fig. 4. Simplified geometrical model used to estimate the collapse top displacement of RC
 192 building

193 *Shear capacity corresponding to Point 2 (V_2)*

194 As depicted in Fig. 5, the base shear V_2 is identified as the intersection of the line CC' and the
 195 capacity curve and can be computed following Eq. (8).

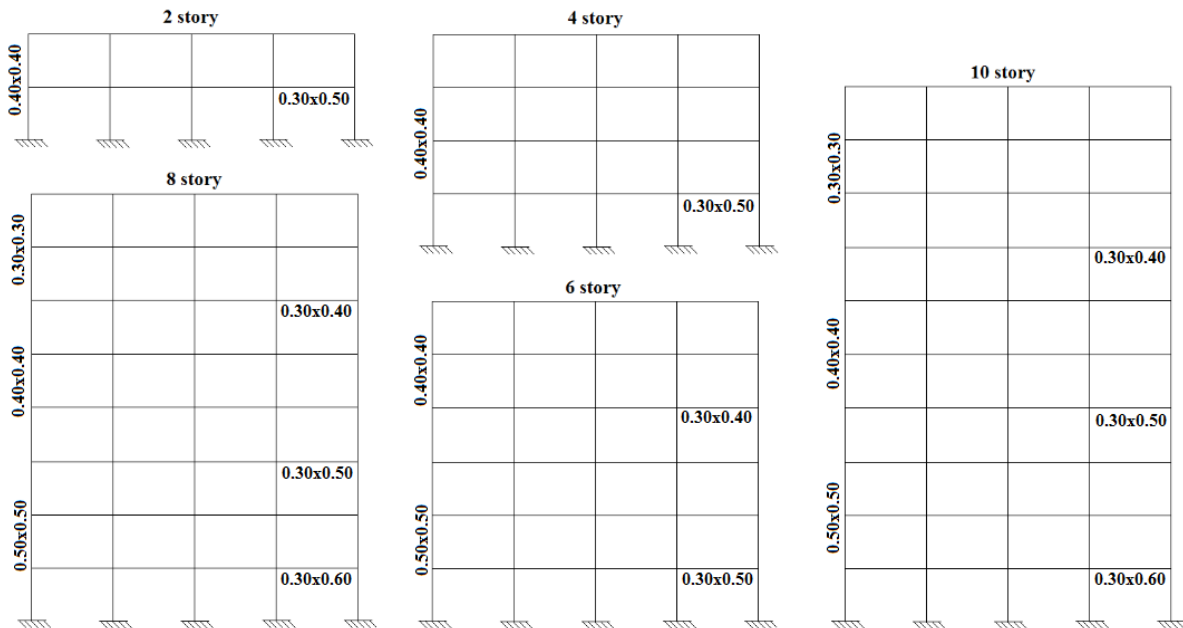
$$196 \quad V_2 = c_2 \cdot \lambda \cdot V_{b,y} \quad (8)$$

197 where c_2 is derived by performing sensitivity analysis considering 220 RC Moment Resisting
 198 Frames (MRF), designed according to general capacity design rules [37] (two, four, six, eight
 199 and ten stories; two, four, six, and eight spans; Fig. 6). Their span length has been fixed to 5.50
 200 m and the story height to 3.00 m. The effect of reinforcement percentage (ρ) on the global shear
 201 capacity has been investigated by assuming two categories: low ($\rho \leq 2\%$) and medium-high
 202 reinforcement rate ($\rho > 2\%$). The models have been developed using SAP2000 [38].



203
204

Fig. 5. Geometrical scheme for Point (2) base shear computation



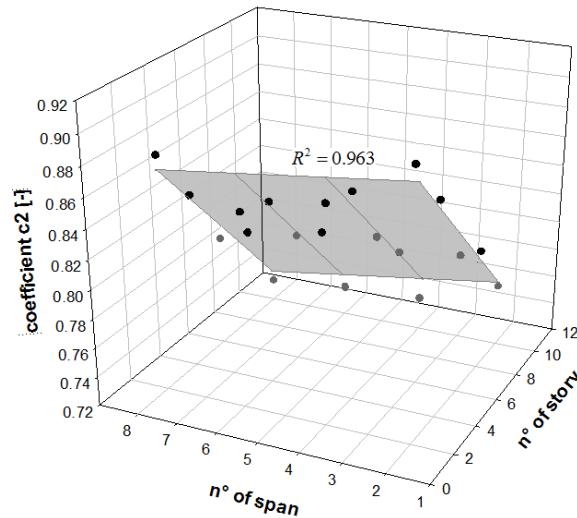
205
206

Fig. 6. Representative 2D frames considered in the sensitivity analysis

207 Masses have been uniformly distributed on each floor and 5% Rayleigh damping has been
 208 considered. Concentrated plasticity model (FEMA 356 type P-M2-M3 for columns and beams),
 209 has been chosen to take into account the nonlinearity in the structural components. The analysis
 210 has been performed by monotonically increasing forces proportional to the equivalent mode, and
 211 considering P-Δ effects. Finally, Eq. (9) allows estimating c_2 coefficient.

212
$$c_2 = 0.0154 \cdot n_{st} - 0.0039 \cdot n_{sp} + 0.925 - (1 - 0.968^{\rho_d}) \quad (9)$$

213 where n_{st} and n_{sp} are the number of stories and spans, respectively, while ρ_d is a dummy variable
 214 that assumes zero value for low reinforcement rate and 1 for medium and high reinforcement
 215 rate. Fig. 7 shows the results of the sensitivity analysis and the measure of goodness fit in terms
 216 of the coefficient of determination (R^2).



217
 218 Fig. 7. Goodness fit measure of Eq. (9)

219 *Top displacements corresponding to the Point 2 and 3 (u_2, u_3)*

220 Displacements u_2 and u_3 are estimated using the equal energy rule and assuming line through
 221 Points (2) and (3) is parallel to that one through Points (1) and (4) (Fig. 8). Therefore, the
 222 equivalent elastic energy (A_{055}) is equal to the elasto-plastic energy (A_{012344}).

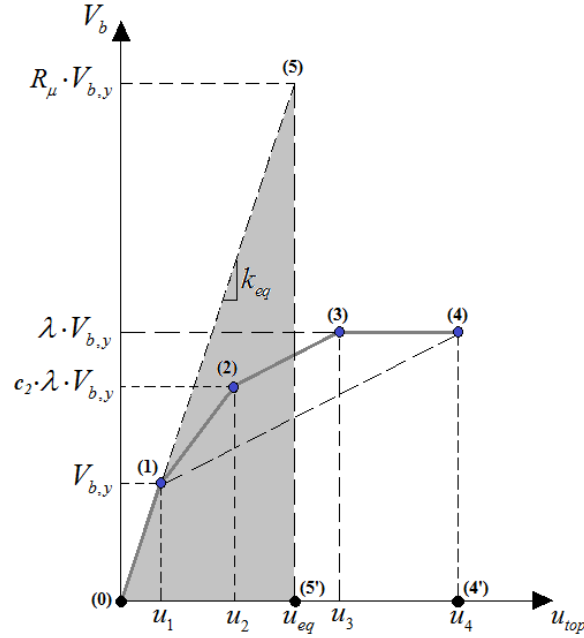


Fig. 8. Illustrative scheme of the physical assumptions

223
224

225 Following the second assumption, u_3 is given by Eq. (10).

226
$$u_3 = u_2 + \frac{u_4 - u_1}{V_{b,y} \cdot (\lambda - 1)} \cdot \lambda \cdot V_{b,y} \cdot (1 - c_2) \quad (10)$$

227 Moreover, equal energy rule is expressed by Eq. (11).

228
$$\frac{(R_\mu \cdot V_{b,y}) \cdot u_{eq}}{2} = V_{b,y} \cdot \left[\lambda \cdot u_4 + \lambda \cdot u_3 \cdot \left(\frac{c_2 - 1}{2} \right) + u_2 \cdot \left(\frac{1 - 3 \cdot c_2 \cdot \lambda}{2} \right) - u_1 \cdot \frac{c_2 \cdot \lambda}{2} \right] \quad (11)$$

229 where R_μ is the reduction factor that is a function of the unknowns u_2 and u_3 , while u_{eq} is the
230 elastic displacement associated with Point (5). Finally, u_2 and u_3 are evaluated by the following
231 iterative procedure:

- 232 - Step 1: A value of the reduction factor is fixed;
233 - Step 2: Eq. (10) is substituted in Eq. (11) and u_2 is calculated;
234 - Step 3: u_3 is assessed through Eq. (10);
235 - Step 4: The following conditions have to be verified (Eq. (12)):

236
$$u_3 < u_4 \quad \text{and} \quad u_2 > \frac{c_2 \cdot \lambda \cdot V_{b,y}}{k_{eq}} \quad (12)$$

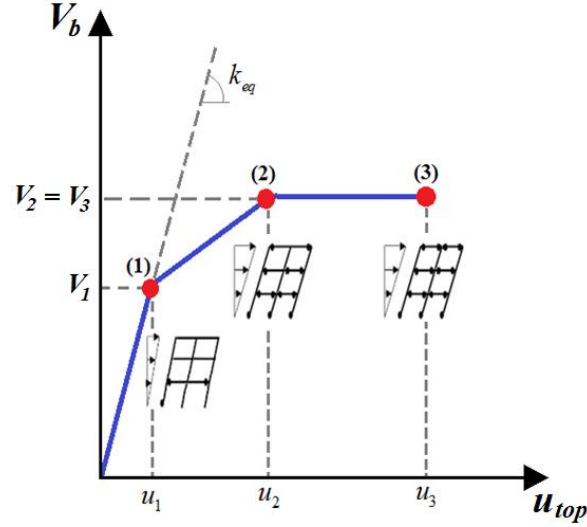
237 - Step 5: If previous conditions are verified, the reduction factor is saved. Otherwise, the
238 procedure from Step 1 to Step 4 has to be repeated.

239 Among all the obtained values of reduction factor, the mean values ($R_{\mu,mean}$) is adopted, and u_2
240 and u_3 , associated with $R_{\mu,mean}$, are evaluated.

241 **2.2 Capacity model for masonry buildings**

242 Masonry buildings are classified as Un-Reinforced Masonry (URM) and Reinforced Masonry
243 (RM). Under seismic actions, a masonry panel is simultaneously subjected to in-plane shear and
244 out-of-plane bending [39] that can lead to different collapse mechanisms. It is common practice
245 to consider only in-plane mechanisms in the global analysis of masonry structures since the out-
246 of-plane mechanisms usually involve parts of the structure that does not affect significantly the
247 global response [40].

248 A simplified methodology based on the Equivalent Frame Model (EFM) is used to reproduce the
249 seismic response of both URM and RM buildings. Panels are idealized as frames composed of
250 deformable vertical (piers) and horizontal (spandrels) elements connected through rigid nodes.
251 Piers are the main resisting elements that carry vertical and horizontal loads, while spandrels
252 affect the boundary conditions of the piers. *Strong spandrels-weak piers model* and *weak*
253 *spandrels-strong piers model* can be adopted for seismic analysis. The nonlinear seismic
254 response is simulated through the tri-linear backbone curve in Fig. 9, similarly to the RC frame
255 model.



256
257

Fig. 9. Proposed tri-linear backbone curve of the global capacity of masonry buildings

258 2.2.1 Elastic parameters at Point (1)

259 A uniform and regular distribution of the openings on the panel is assumed, which is reasonable
260 with typical Italian masonry housing stock [41]. A coupled shear-flexure behavior is considered
261 for the piers, and the related equivalent lateral stiffness ($k_{i,h}$) is derived by Eq. (13).

262

$$k_{ih} = \frac{1}{h_i^3 / (3 \cdot E_i \cdot I_i) + 1.2 \cdot h_i / (G_i \cdot A_i)} \quad (13)$$

263 where E_i and G_i represent the longitudinal and shear elastic modulus, respectively. The principal
264 moment of inertia is expressed by I_i , whereas A_i is the cross-section area of the pier, while h_i
265 refers to the effective height of the pier, according to Dolce [42]. The multimodal approach used
266 to assess the global yield parameters of the RC buildings is adopted also for the masonry
267 building.

268 Different failure mechanisms are proposed in the literature to model the piers and spandrels
269 behavior. A shear failure with diagonal cracks (i), horizontal sliding (ii), and a rocking failure
270 (iii) are herein assumed. Force-deformation relationships (Fig. 10) to model the elastic and
271 plastic behavior are considered for the shear-based and the rocking-based mechanisms.

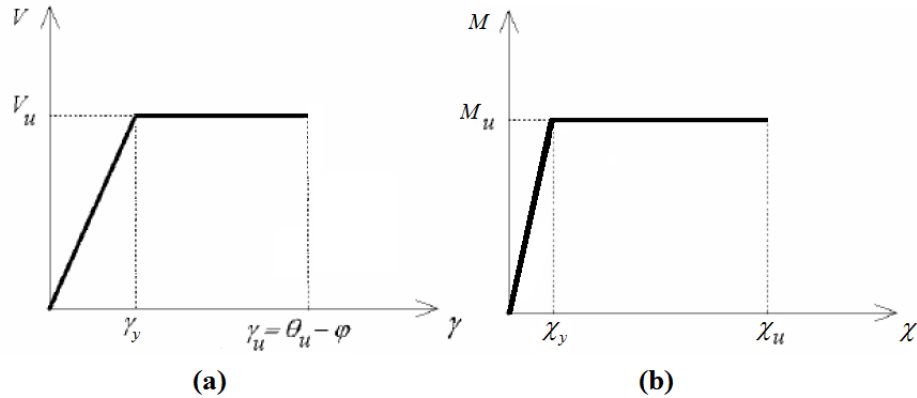


Fig. 10. Shear (a) and rocking (b) behavior of masonry elements

272
273

274 M_u and V_u represent the maximum flexural and shear (diagonal and horizontal) resistance of
 275 masonry elements, respectively. Bending moment capacity is assessed according to the Italian
 276 standard [37] which takes into account the interaction between bending moment and axial load.
 277 Diagonal shear capacity is estimated using the model proposed by [43], while the Mohr-
 278 Coloumb failure criterion is adopted to evaluate the horizontal shear capacity.

279 The shear capacity of the spandrels depends on the model used to simulate the piers-spandrels
 280 behavior. The model proposed by Rizzano, Sabatino [44] is assumed to include the influence of
 281 the spandrels on the global seismic behavior. Assuming weak spandrels model, the maximum
 282 shear capacity can be inferred by imposing local equilibrium, while for strong spandrels model
 283 the element is assumed as a rigid body. Depending on the piers-spandrels interaction model and
 284 the verified failure mechanism, the maximum capacity of each masonry element is estimated
 285 (Fig. 11).

	Maximum Bending capacity	Maximum Shear capacity	
		Diagonal shear	Sliding shear
Pier	$M_u = \left(\frac{\sigma_m \cdot t \cdot D^2}{2} \right) \cdot \left(1 - \frac{\sigma_m}{0.85 \cdot f_m} \right)$ (NTC08, 2008)	$V_u = \frac{f_{td} \cdot t \cdot D}{\beta} \cdot \sqrt{1 + \frac{\sigma_m}{f_{td}}}$ (Turnsek et al., 1971)	$V_u = D_c \cdot t \cdot (\tau_k + 0.4 \cdot \sigma_{mc})$ (Mohr-Coloumb)
Weak spandrel	$M_u = \left(\frac{f_{hd} \cdot t \cdot D^2}{2} \right) \cdot \left(1 - \frac{f_{hd}}{0.85 \cdot f_{hk}} \right)$ (NTC08, 2008)	$V_u = 2 \cdot \frac{M_u}{l_c}$ (Local equilibrium)	—

Fig. 11. Mathematical expression adopted to assess the shear and bending moment resistance both for piers and “weak” spandrels

Variable σ_m is the ultimate axial load ratio that is given by the ratio between the ultimate compression load (N_u) and the cross-section area of the pier; f_{hd} represents the ratio between the ultimate horizontal compression load (N_{uh}) and the cross-section area of the pier; f_m and f_{hk} represent the compression strength and the horizontal compression strength, respectively. The diagonal shear strength is represented by f_{td} , while the coefficient β is assumed equal to 1.5 for slender piers ($\lambda_p \geq 1.5$) and 1 for rigid piers ($\lambda_p < 1.5$). The sliding shear capacity of the pier is proportional to the equivalent compression zone of the pier (D_c) and the sliding shear strength, which is given by the sum of the characteristic shear strength (τ_k) and 40% of the axial load ratio (σ_{mc}).

2.2.2 Post-elastic parameters (Points (2), and (3))

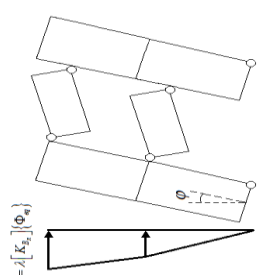
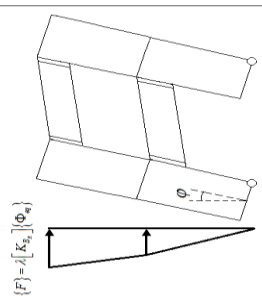
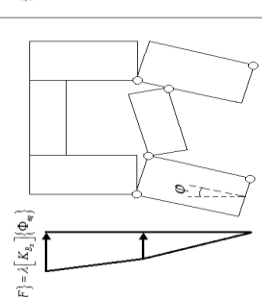
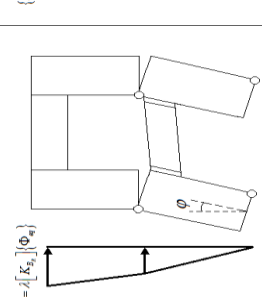
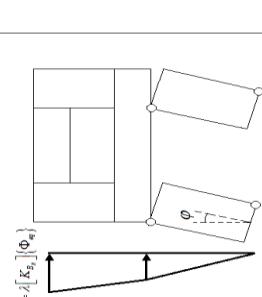
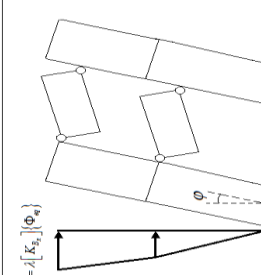
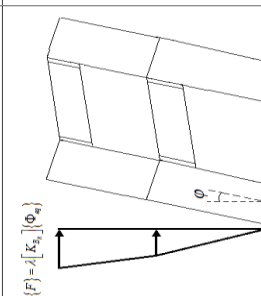
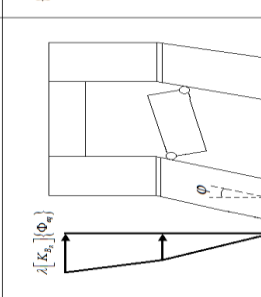
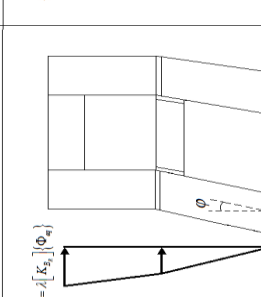
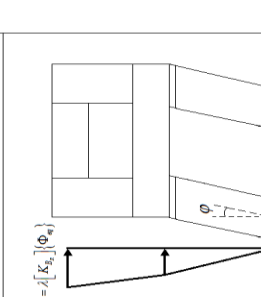
In the following, the post-elastic behavior of the backbone curve is presented through an inverse approach.

Maximum shear capacity ($V_2=V_3$)

The maximum shear capacity ($V_2=V_3$ in Fig. 9) is estimated through the kinematic theorem of limit analysis. Different elementary in-plane collapse mechanisms can be identified considering

304 the pier-spandrel interaction model and on the formation of flexural or shear plastic hinges (Fig.
305 12).

306 The index i represents the i^{th} story level and j identifies the j^{th} weakest story where the plastic
307 hinge forms. Accordingly, $M_{pu,i}$ and $M_{su,i}$ are the ultimate moments, while $V_{pu,i}$ and $V_{su,i}$ the
308 ultimate shear forces. The denominators in Fig. 12 refers to the external work due to the
309 horizontal force distribution, while n_p and $n_{s,pl,i}$ represent the number of plasticized piers and
310 spandrels for the i^{th} story level.

SPANDREL				
Bending failure	Shear failure	Bending failure	Shear failure	—
 <p>$\{F\} = \lambda [K_s] \{\Phi_s\}$</p> $\lambda = \frac{\sum_{s=1}^{df} n_p M_{s,sj} l_s + 2 \sum_{s=1}^{df} n_{p,j} M_{s,sj}}{\sum_{s=1}^{df} F_s (z_s - z_p)}$	 <p>$\{F\} = \lambda [K_s] \{\Phi_s\}$</p> $\lambda = \frac{n_p M_{s,sj} l_s + \sum_{s=1}^{df} n_{p,j} V_{s,sj} l_s}{\sum_{s=1}^{df} F_s (z_s - z_p)}$	 <p>$\{F\} = \lambda [K_s] \{\Phi_s\}$</p> $\lambda = \frac{2 n_p M_{s,sj} + 2 n_{p,j} M_{s,sj}}{h \sum_{s=1}^{df} F_s}$	 <p>$\{F\} = \lambda [K_s] \{\Phi_s\}$</p> $\lambda = \frac{n_p V_{s,sj} l_s + n_{p,j} V_{s,sj} l_s}{h \sum_{s=1}^{df} F_s}$	 <p>$\{F\} = \lambda [K_s] \{\Phi_s\}$</p> $\lambda = \frac{2 n_p M_{s,sj}}{h \sum_{s=1}^{df} F_s}$
 <p>$\{F\} = \lambda [K_s] \{\Phi_s\}$</p> $\lambda = \frac{0.5 n_p V_{s,sj} l_s + \sum_{s=1}^{df} 2 n_{p,j} M_{s,sj}}{\sum_{s=1}^{df} F_s (z_s - z_p)}$	 <p>$\{F\} = \lambda [K_s] \{\Phi_s\}$</p> $\lambda = \frac{0.5 n_p V_{s,sj} l_s + \sum_{s=1}^{df} n_{p,j} V_{s,sj} l_s}{\sum_{s=1}^{df} F_s (z_s - z_p)}$	 <p>$\lambda [K_s] \{\Phi_s\}$</p> $\lambda = \frac{n_p V_{s,sj} l_s + 2 n_{p,j} M_{s,sj}}{h \sum_{s=1}^{df} F_s}$	 <p>$\{F\} = \lambda [K_s] \{\Phi_s\}$</p> $\lambda = \frac{n_p V_{s,sj} l_s + n_{p,j} V_{s,sj} l_s}{h \sum_{s=1}^{df} F_s}$	 <p>$\{F\} = \lambda [K_s] \{\Phi_s\}$</p> $\lambda = \frac{n_p V_{s,sj} l_s}{h \sum_{s=1}^{df} F_s}$
Bending failure		Shear failure		
PIER				
GLOBAL MECHANISM (strong pier-weak spandrel)		LOCAL MECHANISM (strong pier-weak spandrel)		LOCAL MECHANISM (weak pier-strong spandrel)

311
312
313

Fig. 12. Possible collapse mechanisms for weak spandrels-strong pier and weak pier-strong spandrels model considering shear and flexural plastic hinges and associated collapse multipliers

314 *Ultimate collapse displacement (u_3)*

315 The geometrical model proposed for RC building (Fig. 4) is used to evaluate u_3 . The ultimate
316 chord rotation values are assumed 0.6% in case of rocking failure and 0.4% in the case of shear
317 failure [45].

318 *Top displacement corresponding to the extensive damage (u_2)*

319 The iterative procedure used for RC building is herein adopted to evaluate u_2 following the equal
320 energy rule.

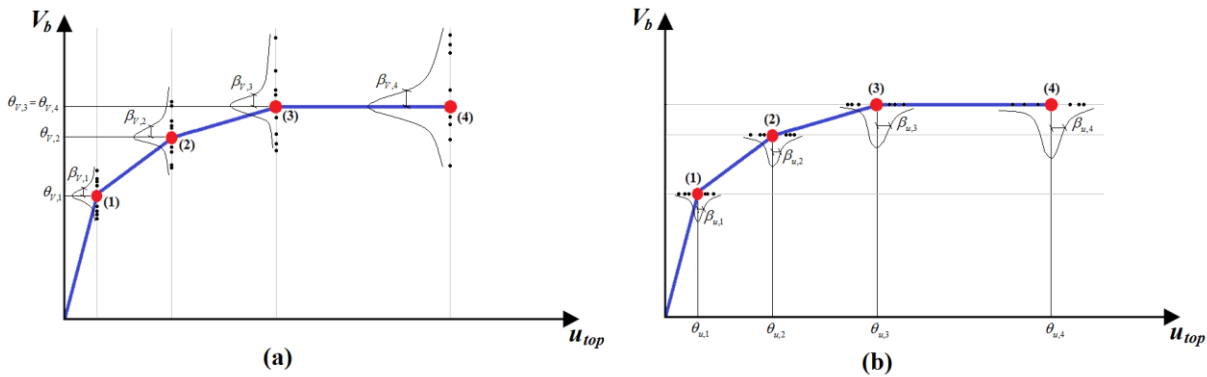
321 **2.3 Modeling uncertainties**

322 Most of the structural parameters are random, and consequently, uncertainties exist in the
323 behavior of the structural members [46]. Backbone curves are herein estimated assuming each
324 parameter as normally distributed Random Variable (RVs). Furthermore, the correlation between
325 variables is considered through multivariate normal distributions.

326 The year of construction is an essential property of each building. It affects the definition of
327 certain structural, nonstructural, and geometrical parameters. In the proposed computational
328 framework, each normally distributed building attribute is defined through a mean (μ) and a
329 standard deviation (σ) based on the year of construction. The mean building attributes are
330 assigned based on the values proposed by the design codes for a given year of construction,
331 while the standard deviations reflect the lack of knowledge in the definition of the building's
332 attributes. Based on that, the standard deviation values increase with the building's age.

333 Monte Carlo Simulations (MCS) are first performed to provide a probabilistic estimate of
334 building behavior. Then a lognormal distribution is adopted to estimate structural capacity. The
335 number of MCS iterations (n_{STEP}) is fixed when a stable estimate of the distribution parameters

336 (median θ_i and dispersion β_i) is verified (Fig. 13). The median backbone curve representative of
 337 the global seismic response of individual building is characterized by the envelope of the median
 338 pairs of base shear and top displacement values.



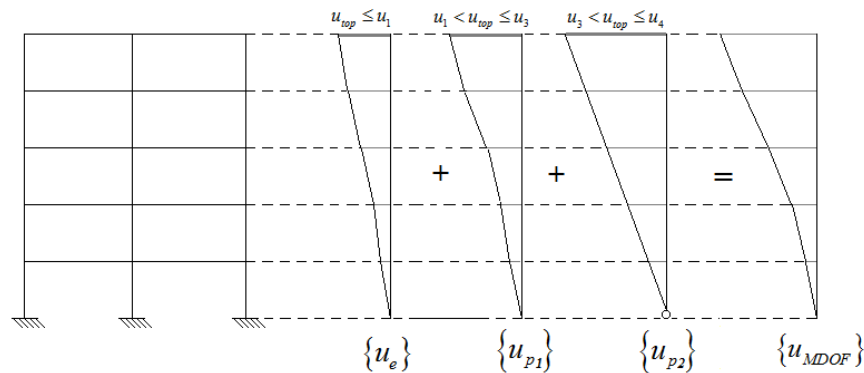
339 Fig. 13. Dispersions associated with the base shear (a) and top displacements (b) for an RC
 340 building
 341

342 3. DAMAGE ASSESSMENT

343 Following HAZUS [47], seismic damage is herein established on deformation criteria and can be
 344 classified in five Damage States (DSs): *none*, *slight*, *moderate*, *extensive*, and *complete damage*,
 345 with respect to different inter-story drift levels. To identify the inter-story drift associated to each
 346 DS the approach proposed by Ghobarah [48] has been considered, where both RC concrete and
 347 masonry buildings are classified into ductile and non-ductile systems according to their energy
 348 dissipation capacity.

349 Nonlinear time-history analyses are performed by modeling for each buildings adopting the
 350 surrogated model, using the median backbone curve and the hysteresis law in both horizontal
 351 directions. Besides, equivalent damping is evaluated according to Rayleigh formulation, while
 352 equivalent mass is concentrated on the top of the systems.

353 Maximum absolute top displacement is a global indicator; therefore it is not representative of the
 354 damage experienced at each story level. On the contrary, according to ATC - 58 [49], the inter-
 355 story drift ratio can be considered as a reasonable parameter to predict seismic performance.
 356 To convert maximum absolute top displacements to maximum inter-story drifts, a simplified
 357 approach is herein adopted. The lateral displacement distribution of individual buildings is
 358 evaluated as the sum of elastic (u_e) and plastic (u_p) contributions (Fig. 14).



359
 360 Fig. 14. Elastic and plastic lateral displacement distributions

361 The first contribution u_e is proportional to the equivalent modal shape. The plastic contribution in
 362 turn is split into u_{p1} and u_{p2} . For sake of simplicity, the first part of the plastic horizontal
 363 displacements is assumed to be proportional to the equivalent modal shape magnified by the ratio
 364 between the initial stiffness k_e and the degraded stiffness connected to the second and the third
 365 part of the backbone curve.

366 The second part u_{p2} is associated with the collapse mechanism. Thus, the lateral displacement
 367 distribution is assumed as directly proportional to the collapse displacement distribution. Fig. 15
 368 resumes the mathematical formulation of the proposed simplified model. Finally, maximum
 369 inter-story drifts are compared with the threshold values of the inter-story drifts proposed by
 370 Ghobarah [48] to assess the damage level.

	RC	Masonry
$u_{top} \leq u_1$	$\{u\} = \{\phi_{eq}\} \cdot u_{top}$	$\{u\} = \{\phi_{eq}\} \cdot u_{top}$
$u_1 < u_{top} \leq u_2$	$\{u\} = \{\phi_{eq}\} \cdot \left[u_1 + (u_{top} - u_1) \cdot \frac{(u_2 - u_1)}{u_1 \cdot (c_2 \cdot \lambda - 1)} \right]$	$\{u\} = \{\phi_{eq}\} \cdot \left[u_1 + (u_{top} - u_1) \cdot \frac{(u_2 - u_1)}{u_1 \cdot (\lambda - 1)} \right]$
$u_2 < u_{top} \leq u_3$	$\{u\} = \{\phi_{eq}\} \cdot \left[u_1 + \frac{(u_2 - u_1)^2}{u_1 \cdot (\lambda \cdot c_2 - 1)} + (u_{top} - u_2) \cdot \frac{(u_3 - u_2)}{u_1 \cdot \lambda \cdot (1 - c_2)} \right]$	$\{u\} = \{\phi_{eq}\} \cdot \left[u_1 + \frac{(u_2 - u_1)^2}{u_1 \cdot (\lambda - 1)} \right] + \{\phi_p\} \cdot (u_{top} - u_2)$
$u_3 < u_{top} \leq u_4$	$\{u\} = \{\phi_{eq}\} \cdot \left[u_1 + \frac{(u_2 - u_1)^2}{u_1 \cdot (\lambda \cdot c_2 - 1)} + \frac{(u_3 - u_2)^2}{u_1 \cdot \lambda \cdot (1 - c_2)} \right] + \{\phi_p\} \cdot (u_{top} - u_3)$	—

Fig. 15 Mathematical formulations to obtain the lateral displacement distribution

4. VALIDATION OF THE SURROGATED MODEL

Three different case studies have been considered to numerically validate the proposed computational framework [38]. The first and second case studies are a five and seven-story RC building with a square and rectangular planar layout, respectively. The third case study is a four-story unreinforced brick masonry building.

The selected case studies have been used to firstly compare the proposed surrogated model with FE-based results. Subsequently, the surrogated model is compared with two existing approaches that are: (i) RISK-UE LM2 [22], and (ii) nonlinear shear MDOF model proposed by Lu and Guan [19].

The first case study has been designed to meet the requirements of capacity design rules and to reproduce the global collapse mechanism. On the contrary, the second case study has been designed to have a soft-story mechanism, by drastically reducing columns stiffness at the fourth story level. Both buildings have a span length of 4.40 m in the x -direction and 6.00 m in y -direction, whereas a story height of 3.00 m is used. The structural members have been designed according to the Italian seismic regulations [37], while the columns are tapered in elevation as shown in Fig. 16.a and Fig. 16.b. A two-ways floor system has been modeled for the two RC frames, while a rigid deck behavior is assumed by releasing both horizontal displacements and

390 the rotation around the vertical axis only. To cope with the reduced flexibility of the frame joints,
391 the rigid links have been adopted by assuming the overlapped beam-column zones as infinitely
392 rigid. A symmetric reinforcement has been adopted for columns and beams in both horizontal
393 directions. A strength class C 30/37 characterizes concrete material, while the B450C strength
394 class has been considered for the steel reinforcements. Steel reinforcement ratios of 2.5 % and
395 1.8 % have been adopted for columns and beams, respectively. Concentrated plasticity model
396 (FEMA 356 type P-M2-M3 for columns and M2-M3 for beams) has been chosen to take into
397 account the nonlinearity in the structural components. Takeda model has been selected for
398 hysteresis behavior. A 5% damping ratio has been assumed according to Rayleigh formulation.

399 The third case study is a four-story unreinforced brick masonry building studied as Equivalent
400 Frame. The walls' thickness is assumed of 0.30 m, while openings have dimensions of 1.30×2.00
401 m. The masonry building has a story height of 4.00 m. The effective length of the piers equals to
402 3.24 m has been evaluated according to Dolce [42]. The deformable length of spandrels is 2.65
403 m, while the width of its cross-section is equal to 0.76 m. A compression strength of 9.40 MPa, a
404 Young modulus of 94000 MPa, and a shear elastic modulus of 37600 MPa have been selected.

405 Shear and flexural plastic hinges have been set based on elastic perfectly plastic force-
406 deformation relationships [38]. Fig. 16 illustrates the 3D models and their structural
407 configuration.

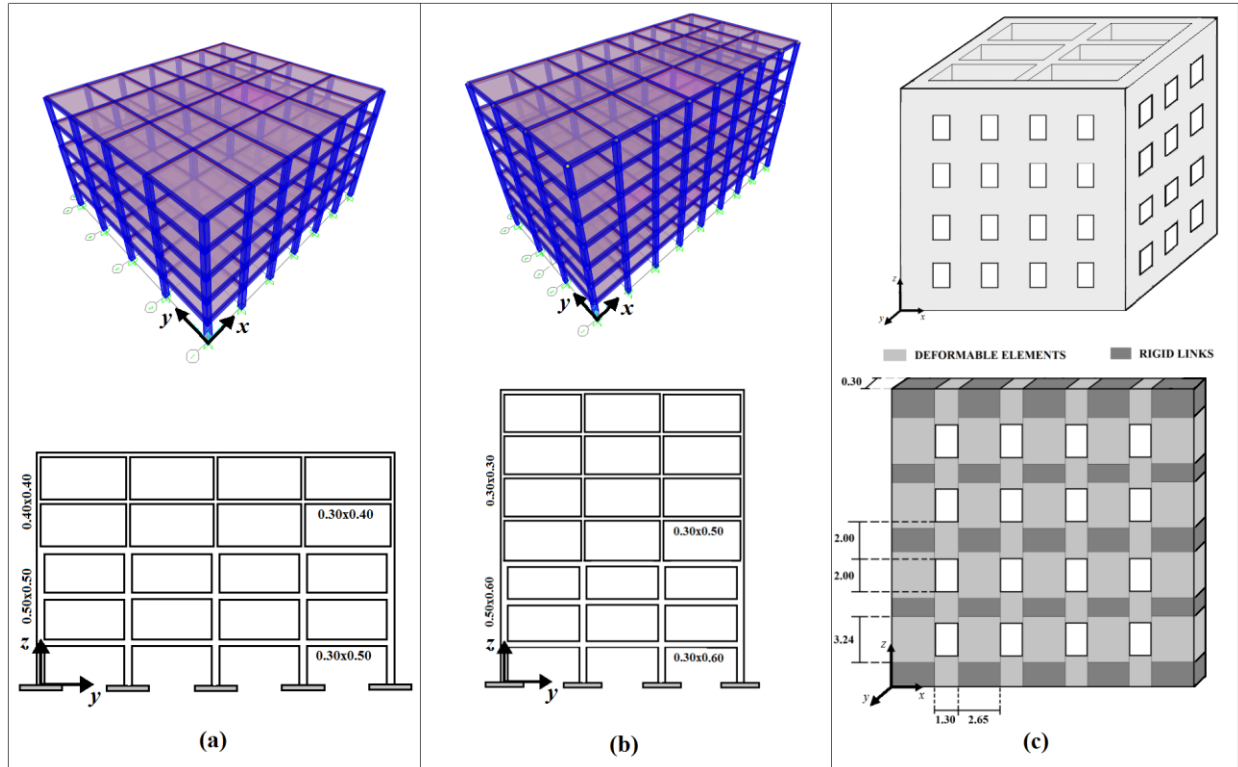


Fig. 16. 3D models and configurations of the first (a), second (b), and third (c) case studies

408
409

410 The comparison between the surrogated and the FE models has been conducted in terms of (i)
411 capacity curves and (ii) dynamic response. Moreover, the capacity curves have been also
412 compared with existing methods (RISK-UE LM2 [22], Lu and Guan [19]).

413 For the three multi-story case studies, the lateral force distributions proportional to the equivalent
414 modal shape have been considered and nonlinear pushover analyses have been performed in both
415 horizontal directions. The material and mechanical parameters have been considered as RVs
416 using their mean values μ_{mat} and μ_{mec} for both surrogated and FE models. The standard
417 deviations associated with the mechanical (σ_{mec}) and material (σ_{mat}) parameters have been set to
418 $0.2 \mu_{mec}$ and $0.15 \mu_{mat}$, respectively [49]. MCSs have been performed with 100 iterative steps,
419 and the median backbone curves have been assessed for both horizontal directions.

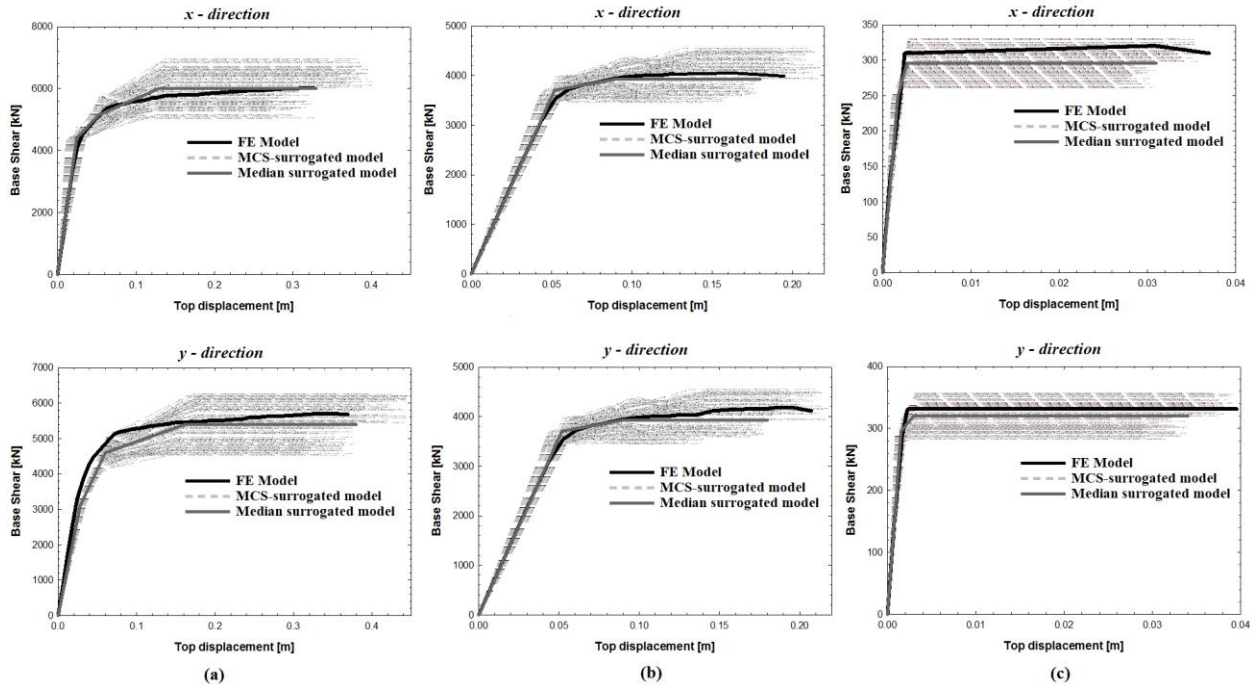
420 To assess the dynamic analysis, the El Centro seismic record has been used as input ground
421 motion [50]. A PGA of 0.61 g has been adopted to clearly show the elastic-plastic response of

422 the Finite Element (FE) models and then compare the results obtained through the proposed
423 surrogated model. The comparisons have been carried out in terms of dynamic displacement
424 response of the top center of the mass of the building in both horizontal directions. Finally,
425 comparisons in terms of maximum inter-story drift are also presented.

426 **4.1 Results**

427 A satisfactory comparison between the capacity curves is shown in Fig. 17. For the second case
428 study, the maximum shear capacity assessed by the proposed methodology is slightly lower than
429 the expected value (Fig. 17b) in both directions. Indeed, because of the soft-story mechanism, the
430 simplified methodology tends to underestimate the collapse multiplier and consequently the
431 maximum shear capacity. Similar considerations are also found for the capacity curve associated
432 with the third case study (Fig. 17c). For the first two case studies, results confirm that
433 considering a four-linear backbone curve increases the accuracy in describing the stiffness
434 degradation beyond the yield point.

435



436
 437 Fig. 17. Comparison between the capacity curves of FE model and estimated backbone curve
 438 derived by using the proposed surrogated model for the first (a), second (b), and third (c)
 439 study building in both horizontal directions

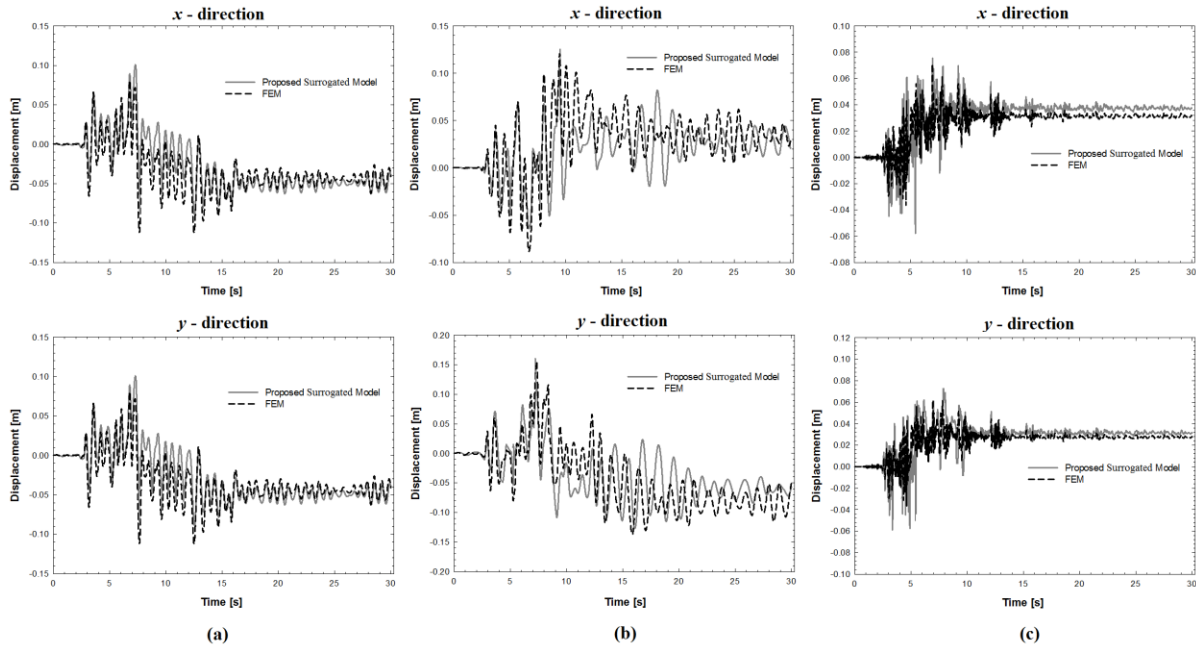
440 Table 1 reports the median and dispersion values of base shear (ϑ_{Vi} , β_{Vi}) and roof displacements
 441 (ϑ_{ui} , β_{ui}) for the first case study building running MCS. Furthermore, the correlation coefficients
 442 (ρ_{Vi-ui}) have been calculated and statistical independency verified.

443 Table 1. Mean and dispersion associated with the base shear and top displacement characteristic
 444 values for the first case study building and related correlation coefficients

	θ		β/θ		ρ
	$V [kN]$	$u [m]$	V	u	
Point 1	4405	0.022	0.040	0.051	-0.001
Point 2	5219	0.045	0.156	0.142	0.009
Point 3	6056	0.119	0.245	0.190	0.006
Point 4	6350	0.279	0.222	0.271	-0.069

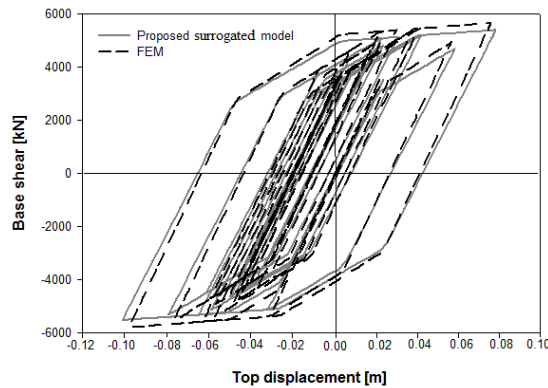
445 Comparisons of the dynamic response in terms of top displacement are depicted in Fig. 18. For
 446 the first case study, the results show a satisfactory accuracy of the surrogated model in predicting
 447 both the dynamic response and residual deformation. For the second and third case studies, due

448 to the soft-story mechanism, some differences have been captured when plastic deformations
449 occur (Fig. 18b and Fig. 18c).



450
451 Fig. 18. Comparison of the dynamic response in term of top displacements for the first (a),
452 second (b), and third (c) case study building in both horizontal directions

453 An additional satisfactory comparison has been provided in Fig. 19 to verify the hysteresis
454 behavior.



455
456 Fig. 19. Comparison of the hysteretic loop for the first case study building between the FE model
457 and proposed model

458 Maximum inter-story drifts are evaluated for both the surrogated and FE model and presented in
459 Table 2. The error in evaluating the maximum drift ratio results in the range of 0-9 %.

460 Table 2. Maximum inter-story drifts assessed through the proposed surrogated and FE models

	Direction	FE model	Proposed model	Error [%]
Case study 1	X	0.92	1.01	9.78
	Y	0.94	0.88	-6.38
Case study 2	X	1.57	1.58	0.64
	Y	3.02	2.87	-4.97
Case study 3	X	1.79	1.90	6.15
	Y	1.63	1.75	7.36

461

462 4.2 Comparisons with existing methods

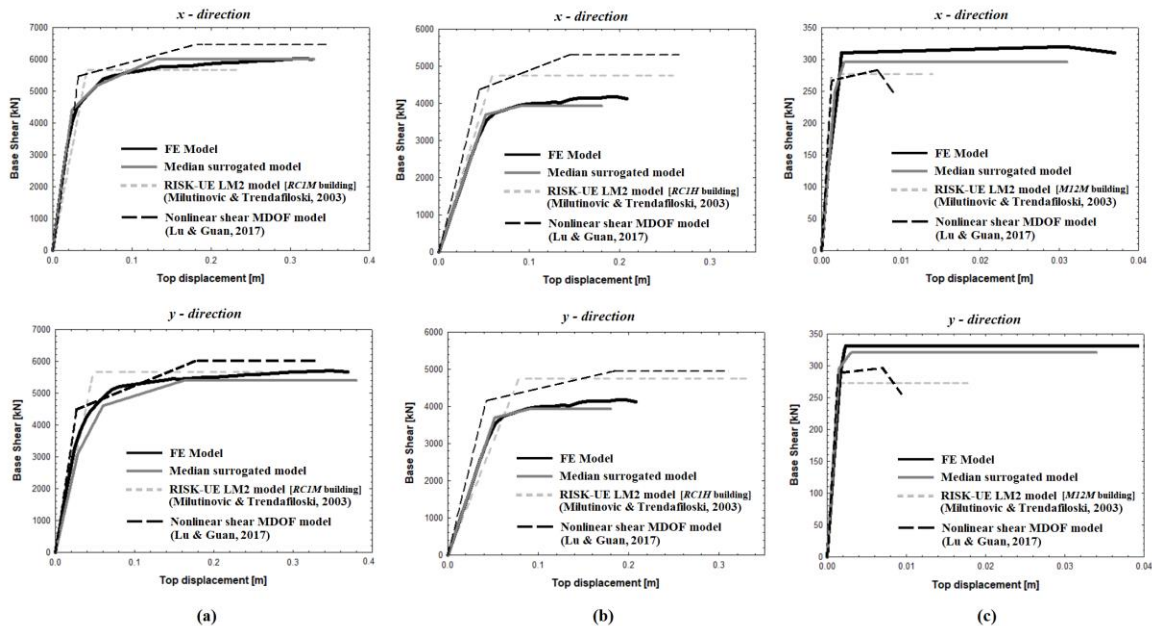
463 The capacity curves of the three case studies have been computed by using the RISK-UE LM2
 464 method [22] and the approach proposed by Lu and Guan [19]. The first method aims at
 465 identifying a bilinear capacity curve, while the second one is based on the definition of a tri-
 466 linear backbone curve.

467 RISK-UE method defines the yield shear as a function of the design strength coefficient and the
 468 overstrength factor that relates the design strength to the real yield strength. The displacement
 469 associated with the yield point is determined based on the first period of vibration. Therefore, the
 470 ultimate shear and displacement are determined based on the overstrength and ductility factors.
 471 All the aforementioned coefficients are related to standard requirements. EC8 provisions [51] are
 472 herein adopted to determine the parameters which allow to evaluate the bilinear capacity curve.

473 Lu and Guan [19] proposed an MDOF lumped mass model where the seismic response is
 474 dominated by the inter-story shear deformation. A tri-linear backbone curve is adopted to
 475 simulate the capacity of the building where the characteristics parameters are determined based
 476 on the Chinese design codes and the statistical data obtained from the experimental and
 477 analytical studies.

478 The capacity curve of the two considered existing approaches are computed by assuming the
 479 same mean values of the geometrical, mechanical, and construction attributes adopted for the

480 surrogated model. Fig. 20 illustrates the comparisons among different approaches of the capacity
 481 curves for the three case study buildings in both horizontal directions. For RISK-UE LM2 model,
 482 the first case study corresponds to Mid-rise Reinforced Concrete Moment Frame (RC1M), the
 483 second case study corresponds to High-rise Reinforced Concrete Moment Frame (RC1H), while
 484 the third case study corresponds to Mid-rise Unreinforced masonry Simple Stone (M12M).



485 (a) (b) (c)

486 Fig. 20. Comparison between the capacity curves of FE model, proposed surrogated model,
 487 RISK-UE LM2 model [22], and Lu and Guan [19] model for the first (a), second (b), and third
 488 (c) case study building in both horizontal directions

489

490 All the capacity curves obtained for the first case study building shows comparable results in
 491 terms of both shear forces and displacements (Fig. 20.a). This can be justified by the building
 492 regularity both in plan and elevation that ensure the conformity of the design parameters.
 493 Furthermore, the use of a four-linear back-bone curve for the surrogated model leads to
 494 accurately model the post-yield characteristics of the capacity curve, while the two considered

495 methods (RISK-UE LM2 [22] and Lu and Guan [19]) do not provide consistent capacity
496 estimates.

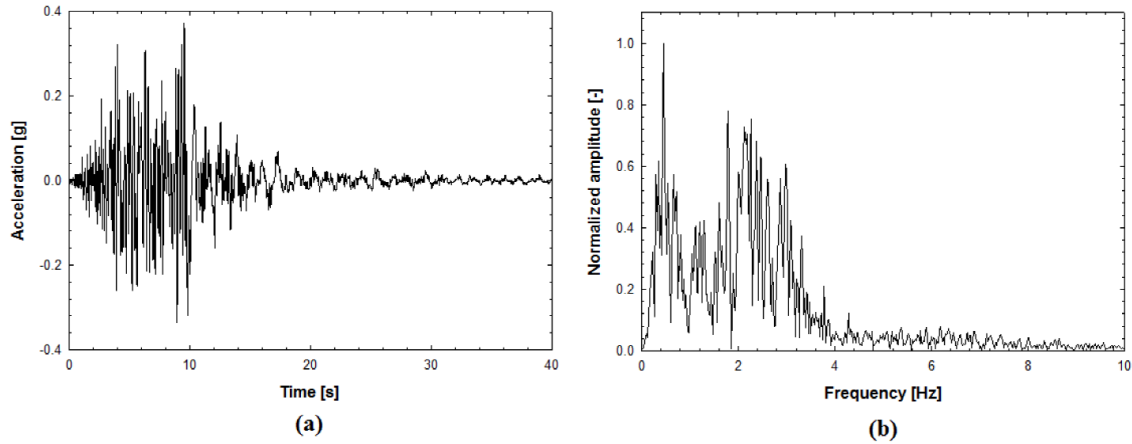
497 Considering the second case study, the two approaches (RISK-UE LM2 [22] and Lu and Guan
498 [19]) provide an overestimation of the building strength and ductility, while the proposed
499 surrogated model is consistent with the FE-based capacity curve. These discrepancies are caused
500 by the stiffness irregularity of the building leading to a local collapse mechanism. Indeed, the
501 design requirements adopted to evaluate the post-elastic coefficients for RISK-UE LM2 [22] and
502 Lu and Guan [19] models are essentially based on regular structure, leading to overestimate the
503 shear capacity and the ultimate collapse displacement (Fig. 20.b).

504 Finally, the capacity curves associated to the third case study and computed with RISK-UE LM2
505 [22] and Lu and Guan [19] models show an underestimation of the ultimate deformation and
506 shear capacity (Fig. 20.c). Therefore, they tend to model the post-elastic masonry behavior with
507 low ductile capacity, with respect to the proposed surrogated model.

508 **5. COMPARISON WITH REAL POST-EARTHQUAKE SCENARIO**

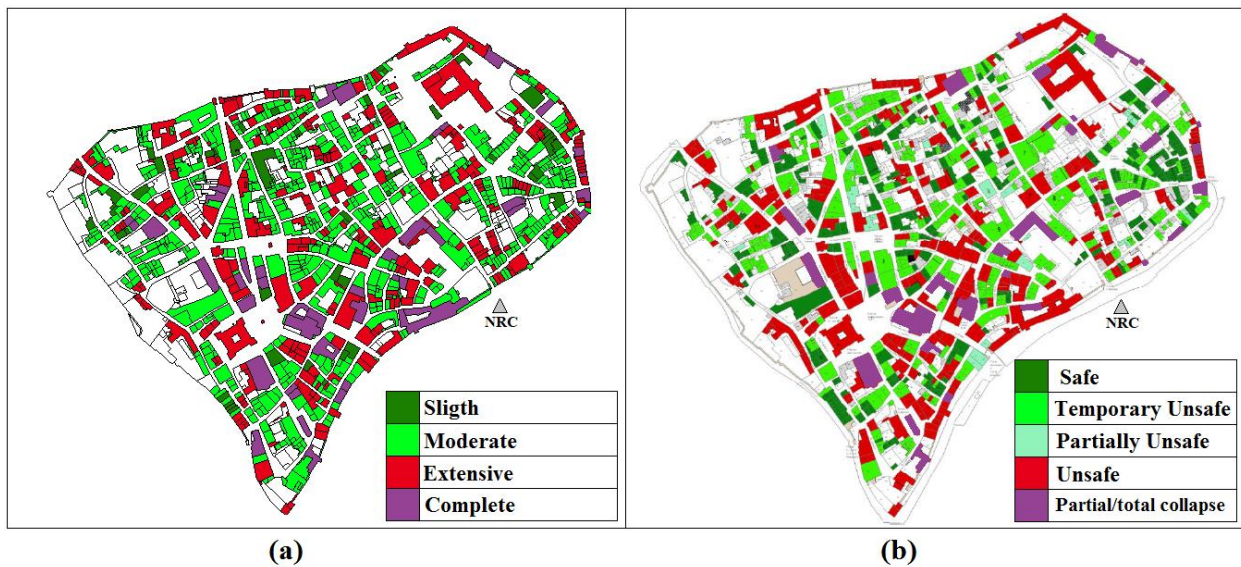
509 In this section, comparison of the proposed surrogated model with a real post-earthquake
510 scenario is provided for validation. It consists of damage data of downtown of the Municipality
511 of Norcia after the seismic event of Central Italy (6.5 Mw, 2016/10/30) [52]. The building stock
512 is composed of 719 buildings including 95% masonry and 5% RC buildings from one to four
513 story levels. About 56% of the buildings were built before 1919, while most of them have been
514 retrofitted after the seismic events of 1971, 1979, and 1997. The building stock is classified
515 based on their structural configuration, geometry, quality of the members, and retrofitting
516 actions.

517 Post-earthquake damage data has been collected through the survey conducted by Italian Civil
518 Protection. Accordingly, buildings have been classified as unsafe, partially unsafe, temporary
519 unsafe, and safe. This classification is based on the building practicability after seismic events
520 depending on structural and nonstructural damage, and proximity with other structurally unsafe
521 buildings [53]. A building is considered unsafe or partially unsafe when the entire building or
522 part of it is significantly damaged and then life-safety is at risk. Based on this definition,
523 unsafe and partially unsafe states may be considered as equivalent to extensive damage state
524 [47]. A building is classified as temporary unsafe when limited structural damage occurs
525 without compromising life safety and it can return safely through simple rapid actions.
526 Therefore, a temporary unsafe condition is comparable with a moderate damage state.
527 Finally, safe conditions represent fully operational levels where the life risk is null, which
528 can be assumed as a slight damage state. Furthermore, partial and total buildings' collapse
529 reported in the survey are considered a complete damage state. The proposed surrogated
530 model is used to assess the damage of each single building located within the downtown
531 area. The seismic scenario has been defined through the horizontal acceleration time histories
532 of the Central Italy earthquake (6.5 Mw, 2016/10/30) recorded in the station of Norcia (NRC in
533 Fig. 22). Fig. 21 illustrates the recorded time history and the frequency content.



534
 535 Fig. 21. (a) North-South acceleration time history recorded in the station of Norcia (NRC) during the
 536 Central Italy earthquake, and (b) the associated frequency content

537 Fig. 22 depicts the comparisons between the results of the numerical simulation and the real
 538 post-earthquake damage scenario. It can be noted satisfactory compatibility between the results,
 539 in particular for complete and extensive DSs, while the small differences are mainly related to
 540 different definitions of the DSs itself and the way the data were collected on-site.



541
 542 Fig. 22. Comparison between the DSs as from the simulations (a) and real post-earthquake
 543 scenario of Norcia (b)

544 A global goodness index has been computed to describe how well the numerical simulations fit
545 the observations. It is estimated giving to each building a value of 1 or 0 if there is an agreement
546 between the simulated damage level and the real observations or not, respectively. Then, the
547 global goodness index is obtained summing each building's index and dividing it by the total
548 number of buildings. A measure of goodness of 83% provides a satisfactory comparison.

549 The raw post-earthquake data herein adopted are in line with the assumptions of the proposed
550 methodology. They report the experienced damage level based on a qualitative approach using a
551 rapid visual screening of each building. However, it is worth noting how the use of raw post-
552 earthquake data may lead to misleading results since the vulnerability of the building portfolio
553 depends on the mutual interactions with the surrounding buildings and infrastructures. Indeed, a
554 building could be considered unsafe even if it experienced low damage due to external causes
555 (e.g. heavy damaged surrounding building, interrupted road access).

556

557 **6. FRAMEWORK APPLICATION TO A LARGE-SCALE VIRTUAL CITY**

558 In this section, the computational framework is applied to a virtual city named "*Ideal City*"[54]
559 that consists of 23420 residential buildings. The building information such as occupancy and
560 physical characteristics of the structures (building archetype, year of construction, and height
561 classifications) have been collected for being representative of the average characteristics of the
562 housing stock of the city of Turin, Italy. The overall area of the city of Turin is around 120 km²
563 with a population of more than 900.000 inhabitants. The building stock of the city is
564 representative of a typical Italian building portfolio. Fig. 23a illustrates the distribution of the
565 buildings based on the archetypes (37% masonry and 63% RC), while Fig. 23b shows the
566 building distribution based on the year of construction.

567 A simplified seismic scenario has been assumed by defining epicenter location, moment
568 magnitude, and time history recorded in the epicenter. Geometrical attenuation at any building
569 location has been estimated based on the Ambraseys model [55], adopting constant frequency
570 content between the stations (buildings). Therefore, the site amplification has been defined in
571 terms of PGA attenuation with the distance to the epicenter. The building-epicenter distances
572 have been evaluated and used in the attenuation relationship as geometrical distance parameter.
573 A stiff soil has been considered to model the ground conditions of the virtual city, where the
574 shear velocity in the uppermost 30 m ranges between 360 and 750 m/s.

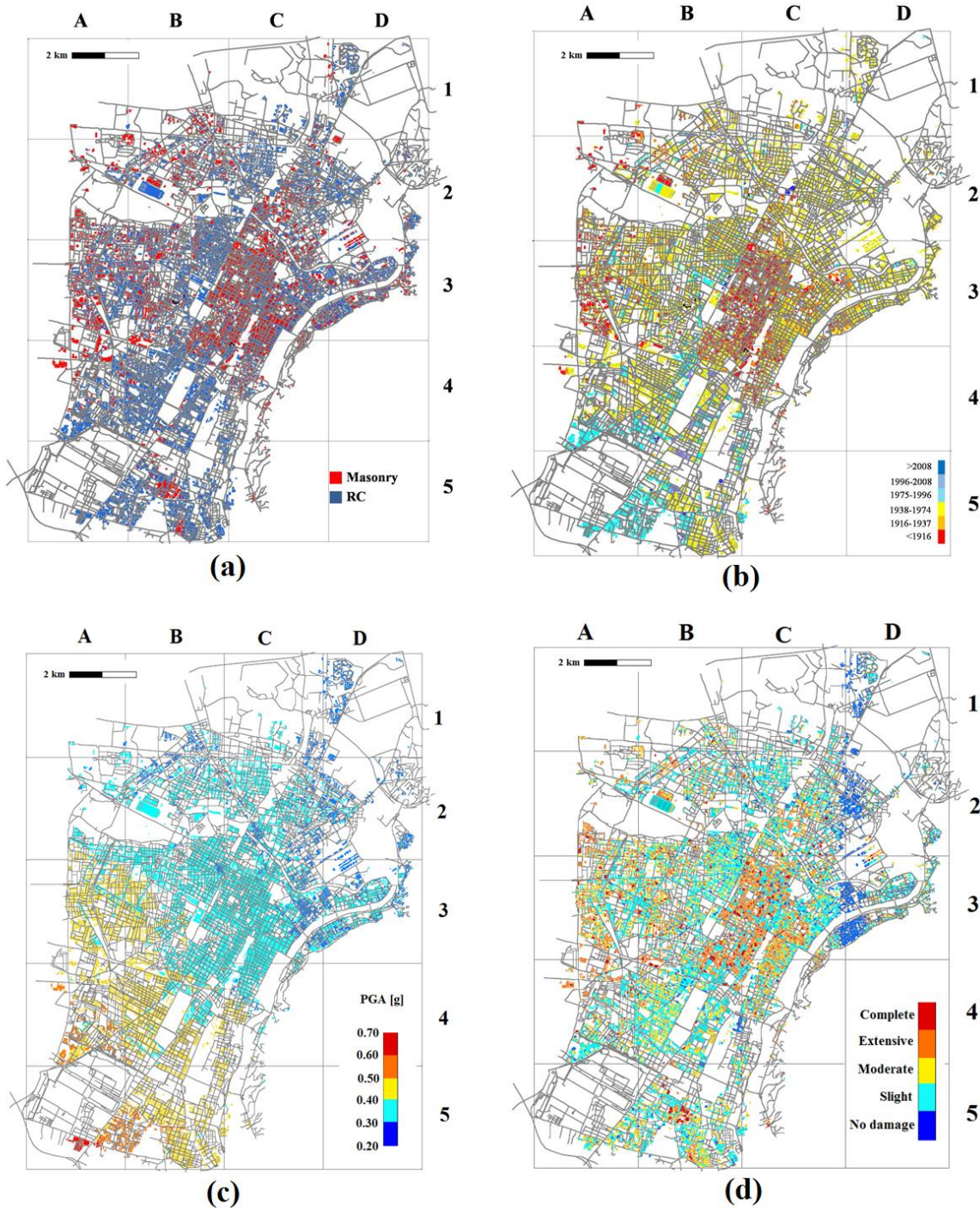
575 The horizontal acceleration time histories of the Central Italy earthquake (6.5 Mw, 2016/10/30)
576 in the station of Norcia (NRC) have been adopted for the analysis (Fig. 21). Fig. 23c shows the
577 map of PGA and the epicenter location. MCSs have been performed using 30 iterations and the
578 median backbone curve has been evaluated for each building. Time history analyses have been
579 then executed and each dynamic building response has been estimated.

580 The computational procedures are performed through a Rack Server with no. 2 Intel Xeon (E5-
581 2698 v4 2.2GHz, 50M Cache, 9.60GT/s QPI, Turbo, HT, 20C/40T (135W) Max Mem
582 2400MHz) and 256 Gb RAM (8x32GB RDIMM, 2400MT/s, Dual Rank, x4 Data Width). To
583 improve the computational performance for large scale simulations, the surrogated model has
584 been implemented within OpenSees in Python [56]. The measured running time has been
585 estimated in about 16 minutes for the entire “*Ideal City*”.

586 Fig. 23d depicts the map of the damage experienced by the buildings [48]. The results show that
587 downtown (C3 in Fig. 23d) is mainly composed of old masonry buildings (see Fig. 23a) and it is the
588 most vulnerable zone. The spatial distribution of the building archetypes (see Fig. 23a) confirms that
589 vulnerability distribution is higher in the zones where the older buildings are located (Fig. 23b) since

590 they were not designed according to updated seismic design requirements. The results confirm that
591 the damage is mostly experienced by masonry buildings rather than RC ones.

592

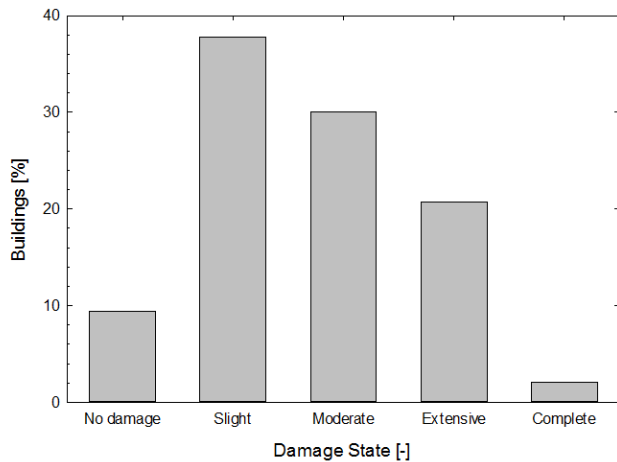


593

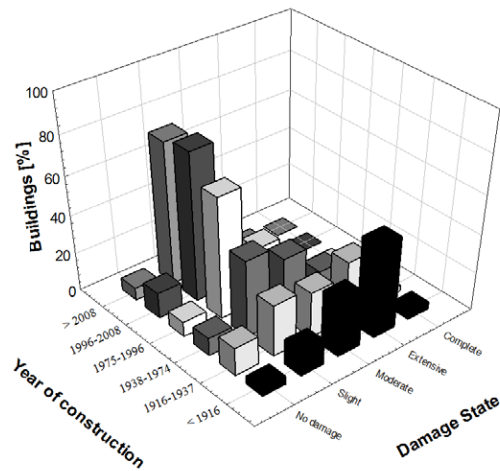
594 Fig. 23. Distribution of buildings within “Ideal City” based on building archetype (a), year of
 595 construction (b), seismic excitation in terms of PGA (c), and level of damage (d). The star
 596 indicates the epicenter location.

597 Furthermore, the total percentages of buildings associated with each DS have been calculated
 598 and reported in Fig. 24a. Most of the buildings have experienced slight damage (about 38 %),
 599 while 30 % and 22 % of the buildings experienced moderate and extensive damage, respectively.
 600 Only 3 % of the buildings are collapsed, whereas the remaining part is undamaged (about 9 %).
 601 The distribution of damaged buildings and the year of construction is shown in Fig. 24b.

602



(a)



(b)

603
 604 Fig. 24. Buildings’ damage distribution (a) and percentage distribution based on year of
 605 constructions (b) within “Ideal City”.

606 Results show that most of the buildings built before 1916 (e.g., coordinates C3 in Fig. 23b) have
 607 experienced extensive damage, although more distant from the epicenter, than newest buildings
 608 (A5 in Fig. 23b), designed with more stringent seismic design requirements, although closer to
 609 the epicenter, which show slight damage.

610 **7. CONCLUDING REMARKS**

611 The prediction of physical damage and the impact of natural hazards on the building portfolio are
 612 challenging issues for community developers and decision-makers. This work is focused on the

613 numerical assessment of earthquakes impact on urban areas. The seismic capacity of each
614 building has been estimated through a surrogated model. Uncertainties have been included by
615 using the Monte Carlo simulations. Nonlinear time-history analyses have been performed and
616 structural damage has been estimated based on the maximum inter-story drift. The proposed
617 surrogated model, suitable both for RC and masonry buildings, leads to accurately identify the
618 individual building capacity. The proposed model has been validated using a real post-
619 earthquake scenario. Then, it has been tested on a large-scale city, showing a direct
620 proportionality between the experienced damage to the buildings category and their age.
621 Moreover, masonry buildings were found to be more vulnerable than RC buildings.
622 The surrogated nonlinear model stands at an intermediate level between a detailed description of
623 the built environment and a typological one. It results in computationally effective and providing
624 an accurate estimate considering both the individual building characteristics and the inherent
625 uncertainties. The limited computational demand and the clear representation of the output
626 scenario make the surrogate model a useful tool for a rapid assessment of the damage by
627 decision-makers, even those that are not experts in the field.

628 **ACKNOWLEDGEMENTS**

629 The research leading to these results has received funding from the European Research Council
630 under the Grant Agreement n° ERC_IDEAL RESCUE_637842 of the project IDEAL
631 RESCUE— Integrated Design and Control of Sustainable Communities During Emergencies.
632 Umbria Region and Municipality of Norcia provided post-earth data with the professional
633 support of Prof. Antonio Borri, University of Perugia. They are gratefully acknowledged.

634 **REFERENCES**

635 [1] Malalgoda C, Amaratunga D, Haigh R. Challenges in creating a disaster resilient built
636 environment. *Procedia Economics and Finance*. 2014;18:736-44.

637 [2] Cimellaro GP, Marasco S. A computer-based environment for processing and selection of
638 seismic ground motion records: OPENSIGNAL. *Frontiers in Built Environment*. 2015;1:17.

639 [3] Kammouh O, Zamani-Noori A, Cimellaro GP, Mahin SA. Resilience Assessment of Urban
640 Communities. *ASCE-ASME Journal of Risk and Uncertainty in Engineering Systems, Part A:
641 Civil Engineering*. 2019;5.

642 [4] Cimellaro, Renschler C, Reinhorn AM, Arendt L. PEOPLES: a framework for evaluating
643 resilience. *Journal of Structural Engineering, ASCE*. 2016;142:1-13 DOI:
644 0.1061/(ASCE)ST.943-541X.0001514.

645 [5] Cimellaro GP, Solari D, Bruneau M. Physical infrastructure Interdependency and regional
646 resilience index after the 2011 Tohoku earthquake in Japan. *Earthquake Engineering &
647 Structural Dynamics*. 2014;43:1763-84.

648 [6] Kammouh O, Dervishaj G, Cimellaro GP. Quantitative framework to assess resilience and
649 risk at the country level. *ASCE-ASME Journal of Risk and Uncertainty in Engineering Systems,
650 Part A: Civil Engineering*. 2018;4:1-14.

651 [7] Cimellaro GP, Scura G, Renschler C, Reinhorn AM, Kim H. Rapid building damage
652 assessment system using mobile phone technology *Earthquake Engineering and Engineering
653 Vibration*. 2014;13:519-33

654 [8] Whitman RV. *Damage Probability Matrices for Prototype buildings; Seismic Design
655 Decision Analysis*. Cambridge, Massachusetts: Massachusetts Institute of Technology; 1973.

656 [9] Rojahn C, Sharpe RL. *Earthquake damage evaluation data for California: Applied technology
657 council*; 1985.

658 [10] Dolce M, Kappos A, Masi A, Penelis G, Vona M. Vulnerability assessment and earthquake
659 damage scenarios of the building stock of Potenza (Southern Italy) using Italian and Greek
660 methodologies. *Engineering Structures*. 2006;28:357-71.

661 [11] Eleftheriadou AK, Karabinis AI. Evaluation of damage probability matrices from
662 observational seismic damage data. *International Journal of Earthquakes and Structures*. 2013;4.

663 [12] Freeman SA. Review of the development of the capacity spectrum method. *ISET Journal of
664 Earthquake Technology*. 2004;41:1-13.

665 [13] Fajfar P, Gašperšič P. The N2 method for the seismic damage analysis of RC buildings.
666 *Earthquake Engineering & Structural Dynamics*. 1996;25:31-46.

667 [14] El Ezz AA, Nolle M-J, Nastev M. Assessment of earthquake-induced damage in Quebec
668 city, Canada. *International journal of disaster risk reduction*. 2015;12:16-24.

669 [15] Korkmaz K. Seismic safety assessment of unreinforced masonry low-rise buildings in
670 Pakistan and its neighbourhood. *Natural Hazards and Earth System Sciences*. 2009;9:1021.

671 [16] Tang B, Lu X, Ye L, Shi W. Evaluation of collapse resistance of RC frame structures for
672 Chinese schools in seismic design categories B and C. *Earthquake engineering and engineering
673 vibration*. 2011;10:369.

674 [17] Vamvatsikos D, Cornell CA. Incremental dynamic analysis. *Earthquake Engineering &
675 Structural Dynamics*. 2002;31:491-514.

676 [18] Xu Z, Lu X, Guan H, Han B, Ren A. Seismic damage simulation in urban areas based on a
677 high-fidelity structural model and a physics engine. *Natural hazards*. 2014;71:1679-93.

678 [19] Lu X, Guan H. *Earthquake disaster simulation of civil infrastructures: from tall buildings to
679 urban areas*: Springer; 2017.

680 [20] Silva V, Crowley H, Pagani M, Monelli D, Pinho R. Development of the OpenQuake
681 engine, the Global Earthquake Model's open-source software for seismic risk assessment.
682 *Natural Hazards*. 2014;72:1409-27.

683 [21] Villar-Vega M, Silva V, Crowley H, Yepes C, Tarque N, Acevedo AB et al. Development
684 of a fragility model for the residential building stock in South America. *Earthquake spectra*.
685 2017;33:581-604.

686 [22] Milutinovic ZV, Trendafiloski GS. Risk-UE An advanced approach to earthquake risk
687 scenarios with applications to different european towns. Contract: EVK4-CT-2000-00014, WP4:
688 Vulnerability of Current Buildings. 2003:1-111.

689 [23] Grünthal G. European macroseismic scale 1998. European Seismological Commission
690 (ESC); 1998.

691 [24] Hori M, Ichimura T, Oguni K. Development of Integrated Earthquake Simulation for
692 estimation of strong ground motion, structural responses and human actions in urban areas.
693 2006:381-92.

694 [25] Hori M, Ichimura T, Wijerathne L, Ohtani H, Chen J, Fujita K et al. Application of high
695 performance computing to earthquake hazard and disaster estimation in urban area. *Frontiers in*
696 *Built Environment*. 2018;4:1.

697 [26] Sahin A, Sisman R, Askan A, Hori M. Development of integrated earthquake simulation
698 system for Istanbul. *Earth, Planets and Space*. 2016;68:115.

699 [27] Cimellaro GP, Marasco S. *Methods of Analysis. Introduction to Dynamics of Structures*
700 *and Earthquake Engineering*; Springer; 2018. p. 331-51.

701 [28] Marasco S, Zamani Noori A, Cimellaro GP. Cascading hazard analysis of a hospital
702 building. *Journal of Structural Engineering*. 2017;143:04017100.

703 [29] Chopra AK, Goel RK. A modal pushover analysis procedure for estimating seismic
704 demands for buildings. *Earthquake engineering & structural dynamics*. 2002;31:561-82.

705 [30] Takeda T, Sozen MA, Nielsen NN. Reinforced concrete response to simulated earthquakes.
706 *Journal of the Structural Division*. 1970;96:2557-73.

707 [31] Cimellaro GP, Giovine T, Lopez-Garcia D. Bidirectional Pushover analysis of irregular
708 structures. *Journal of Structural Engineering, ASCE*. 2014;140:04014059.

709 [32] FEMA. *Prestandard and Commentary for the Seismic Rehabilitation of Buildings*. Federal
710 Emergency Management Agency FEMA 356. Washington, DC: Building Seismic Safety
711 Council; 2000.

712 [33] Kunnath SK. Identification of modal combinations for nonlinear static analysis of building
713 structures. *Computer - Aided Civil and Infrastructure Engineering*. 2004;19:246-59.

714 [34] Guyan RJ. Reduction of stiffness and mass matrices. *AIAA journal*. 1965;3:380-.

715 [35] Neal BG, Symonds PS. THE RAPID CALCULATION OF THE PLASTIC COLLAPSE
716 LOAD FOR A FRAMED STRUCTURE. *Proceedings of the institution of civil engineers*.
717 1952;1:58-71.

718 [36] Greco A, Cannizzaro F, Pluchino A. Seismic collapse prediction of frame structures by
719 means of genetic algorithms. *Engineering Structures*. 2017;143:152-68.

720 [37] NTC. *Normativa Tecnica delle Costruzioni 2018. Progettazione Sismica. Gazzetta Ufficiale*
721 *della Repubblica Italiana*2018.

722 [38] CSI. *Integrated Finite Element Analysis and Design of Structures Basic Analysis Reference*
723 *Manual*. Computers and Structures, Inc, Berkeley, California, USA2018.

724 [39] Maheri MR, Najafgholipour M. In-plane shear and out-of-plane bending capacity
725 interaction in brick masonry walls. *15th World Conference on Earthquake Engineering, Lisbon,*
726 *Portugal*2012.

727 [40] Bucchi F, Arangio S, Bontempi F. Seismic Assessment of an Historical Masonry Building
728 using Nonlinear Static Analysis. 14th International Conference on Civil, Structural and
729 Environmental Engineering Computing. Sardinia, Italy2013.

730 [41] Corrado V, Ballarini I, Corgnati SP. National scientific report on the TABULA activities in
731 Italy. Politecnico di Torino; 2012.

732 [42] Dolce M. Schematizzazione e modellazione per azioni nel piano delle pareti, Corso sul
733 consolidamento degli edifici in muratura in zona sismica. Ordine degli Ingegneri, Potenza (in
734 Italian). 1989.

735 [43] Turnsek V, Cacovi F. Some Experimental Results on the Strength of Brick Masonry Walls.
736 Zavod za Raziskavo Materiala, Konstrukcij, Ljubljana, Yugoslavia. 1971.

737 [44] Rizzano G, Sabatino R, Zambrano M. L'influenza delle fasce di piano sulla resistenza di
738 pareti in muratura. 2009.

739 [45] Bolognini D, Braggio C, Magenes G, terremoti Gnpldd. Metodi semplificati per l'analisi
740 sismica non lineare di edifici in muratura: CNR-Gruppo nazionale per la difesa dai terremoti;
741 2000.

742 [46] Lee T-H, Mosalam KM. Probabilistic fiber element modeling of reinforced concrete
743 structures. Computers & structures. 2004;82:2285-99.

744 [47] FEMA. Hazus: FEMA's methodology for estimating potential losses from disasters. 2011.

745 [48] Ghobarah A. On drift limits associated with different damage levels. Performance-Based
746 Seismic Design Concepts and Implementation: Proceedings of the International Workshop, Bled,
747 Slovenia2004. p. 321-32.

748 [49] ATC - 58. Guidelines for seismic performance assessment of buildings. ATC-58 50% Draft,
749 Applied Technology Council Redwood City, CA; 2009.

750 [50] Chopra AK. Dynamics of structures: theory and applications to earthquake engineering:
751 Prentice-Hall; 2001.

752 [51] Code P. Eurocode 8: Design of structures for earthquake resistance-part 1: general rules,
753 seismic actions and rules for buildings. Brussels: European Committee for Standardization. 2005.

754 [52] Borri A, Sisti R, Prota A, Di Ludovico M, Costantini S, Barluzzi M et al. ANALISI DEL
755 DANNO DEGLI EDIFICI ORDINARI NEL CENTRO STORICO DI NORCIA A SEGUITO
756 DEL SISMA DEL 20162017.

757 [53] AeDES. Manuale per la compilazione della scheda di 1° livello di ri-levamento danno,
758 pronto intervento e agibilità per edifici ordinari nell'emergenza post-sismica Roma: Presidenza
759 del Consiglio dei Ministri. Dipartimento della Protezione Civile.; 2009.

760 [54] Cimellaro GP, Zamani-Noori A, Marasco S, Kammouh O, Domaneschi M, Mahin S. Smart
761 cities to improve resilience of communities. 2nd International Workshop on Modelling of
762 Physical, Economic and Social Systems for Resilience Assessment. Brussels, 14-16 December
763 2017: Joint Research Center in collaboration with NIST; 2017.

764 [55] Ambraseys NN, Simpson Ku, Bommer JJ. Prediction of horizontal response spectra in
765 Europe. Earthquake Engineering & Structural Dynamics. 1996;25:371-400.

766 [56] Zhu M, McKenna F, Scott MH. OpenSeesPy: Python library for the OpenSees finite
767 element framework. SoftwareX. 2018;7:6-11.

768